Wind Turbine Wake Dynamics Analysis Using a High-Fidelity Simulation Framework with Blade-Resolved Turbine Models

Andrew C. Kirby*, Arash Hassanzadeh, Dimitri J. Mavriplis, Jonathan Naughton

Department of Mechanical Engineering, University of Wyoming, Laramie, WY 82071, USA

Analysis of the NREL WindPACT-1.5MW wind turbine is performed under uniform inflow conditions using a high-fidelity numerical simulation with a full rotor model using detailed blade geometry. Analysis is performed using measurements of aerodynamic forces and coefficient of pressure, and wake characteristics are studied using Reynolds stress analysis and Proper Orthogonal Decomposition in the near-wake and mid-wake regions.

I. Introduction

Wind energy is becoming a critical renewable resource for the global energy portfolio as wind turbine designs have grown in scale, thus driving down power production cost.[1] Understanding the aerodynamics of the wind turbine is an essential aspect for energy production optimization, not only for the individual turbine but also for the complete wind farm. Exploration of wind turbine yawing[2–5] for wind farm optimization introduces complex aerodynamics and possible structural effects. These complex aerodynamics, such as flow separation, cannot be captured accurately using lower-fidelity methods, such as actuator disk[6,7] and actuator line[8–10] methods. High-fidelity blade-resolved simulations are required for accurate prediction.

Blade-resolved wind turbine simulations were previously intractable due to immense computational requirements. However, supercomputers have continuously grown by an order of magnitude in computational power approximately every four years[11] making accurate blade-resolved simulations increasingly feasible. One of the first blade-resolved wind turbine simulations was performed by Duque *et al.*[12] in the late 1990s, and development of high-fidelity wind turbine simulation capabilities[13–29] have continued.

The goal of this work is to explore analysis techniques that illuminate the impact of complex blade aerodynamics on wake characteristics. First principles, founded in Newton's third law of motion, imply the wind turbine bodies produce equal and opposite forces on the flow. Thus, wake analysis must incorporate aerodynamic force analysis. Hassanzadeh *et al.*[30] used the concept of Newton's third law to design small-scale wind turbines by matching normalized normal and tangential force distributions of full-scale wind turbines with the goal of matching non-dimensional wake characteristics. Sandia National Laboratory has taken a similar first-principles approach by matching relative circulation.[31] First, this work will measure aerodynamic force distribution and coefficient of pressure on the wind turbine blades to infer the forces that generate the wake, followed by analysis of the wake.

Wind turbines wakes are generally divided into three spatial regions: near-wake, mid-wake, and far-wake. The near-wake region starts at the wind turbine and continues approximately one to three rotor diameters downstream. This region is influenced by the rotor angular velocity and blade geometry and contains distinct blade tip and root vortices. The mid-wake region contains a mixing shear layer and tip vortices that become unstable through vortex merging and hopping, which form into larger flow structures. In the far-wake region, found beyond six rotor diameters downstream, the transition to turbulence occurs as larger vortex flow structures begin to break down into progressively finer turbulence structures. In this work, the turbulence is characterized using Reynolds stress analysis, and the larger wake structures are investigated using Proper Orthogonal Decomposition.

Proper Orthogonal Decomposition (POD), known in Statistics as Principal Component Analysis, is a mathematical transformation used to convert data, possibly correlated, into linearly-independent uncorre-

*Corresponding author: akirby@uwyo.edu

lated components. The first component contains the largest possible variance, and each succeeding component containing less variance. POD is used to construct an uncorrelated orthogonal basis set of the flow structures, allowing lower-dimensional analysis. POD has been applied to turbulent flow problems first by Lumley[32] and later by Sirovich *et al.*[33] and Berkooz *et al.*[34] It has also been used to develop reduced order models for flow problems.[35] POD has recently been used for wind turbine wake analysis in several simulation works,[36,37] and experimental works to study wakes behind bluff bodies.[38] In this work, POD is applied to simulation data extracted from the near-wake and mid-wake regions.

This paper is organized as follows: In Section II, the computational methodology is presented, Section III outlines the wind turbine problem and computational simulation setup, Section IV highlights the analysis approach used for Section V, where the results are presented. Lastly, conclusions are drawn, and future directions are outlined in Section VI.

II. Numerical Methodology

This work utilizes the **W**yoming **W**ind and **A**erospace **A**pplications **K**omputation **E**nvironment (W^2A^2KE3D)[29] framework for high-fidelity blade-resolved wind turbine simulations. The W^2A^2KE3D framework has been applied to several wind energy applications,[28] including a full blade-resolved wind farm simulation[29] containing 48 wind turbines on over 22,000 cores, and it has been scaled up to 144 wind turbines using over 67,000 cores. Additionally, it has been applied to several aerospace applications.[39,40]

W^2A^2KE3D supports multiple computational fluid dynamics (CFD) solvers and multiple computational meshes simultaneously through an overset grid method. The overset mesh system generally consists of a collection of *near-body* and *off-body* meshes as shown in Figure 1. The near-body meshes are inherently unstructured and highly anisotropic, which are used to represent the complex geometry, and resolve the boundary layer of the wind turbine bodies. The off-body mesh is a dynamically adaptive Cartesian grid system, which allows for computationally efficient solvers, efficient storage, and ease of dynamic mesh adaption. This multiple mesh paradigm allows for effective use of solver and mesh technologies in varying flow conditions, particularly in the context of wind energy applications.

The two CFD solvers used in W^2A^2KE3D for this work are NSU3D, the near-body mesh solver, and dg4est, the off-body mesh solver. NSU3D[41,42] is an unstructured finite-volume solver for the Unsteady Reynolds Averaged Navier-Stokes equations. It contains several turbulence models, such as the Spalart-Allmaras (SA),[43] K-Omega,[44] and the Delayed Detached Eddy Simulation (DDES)[45] turbulence models with rotation/curvature correction.[46] The off-body solver, dg4est,[39] is a high-order discontinuous Galerkin finite-element method embedded into the *p4est*[47,48] adaptive mesh refinement framework, and has *hp*-adaption capabilities. It solves the compressible Navier-Stokes Equations, and uses a Constant Smagorinsky Large Eddy Simulation[49] turbulence model. The overset mesh assembler is TIOGA,[50–52] which is used to interpolate solutions between the near-body and off-body meshes.

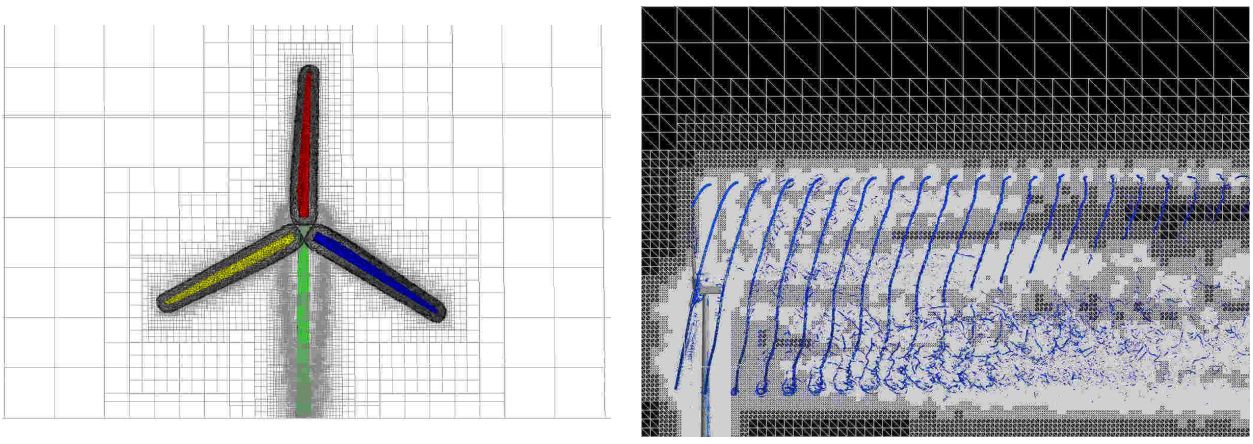

Figure 1. Overset mesh technology used to incorporate complex geometry and effective mesh adaption for wake capturing.

III. Problem Description

This study uses a 1.5MW wind turbine from the NREL Wind Partnership for Advanced Component Technologies[53] (WindPACT) Project, which was used for a turbine rotor study.[54] The WindPACT-1.5MW wind turbine is a three-bladed design with a rotor diameter of 70 m, rotation rate of 20.5 rpm, and an axial velocity of 10.7338 m/s corresponding to a tip-speed ratio of $\lambda = 7.0$. A blade pitch angle of 2.6° is applied with a 0° coning angle.

The rotor geometry is composed of three identical unstructured blade meshes. The unstructured blade mesh is trimmed to approximately 1 meter from the blade surface, as shown in Figure 2. The computational blade mesh is composed of approximately 3.24 million nodes with 687,965 tetrahedra, 49,061 pyramids, and 6,150,915 prisms. The smallest element width is 4.937 microns. The total rotor geometry mesh aggregates to approximately 9.72 million nodes. Each blade mesh is partitioned onto 144 cores, giving a total of 432 cores for the near-body solver.

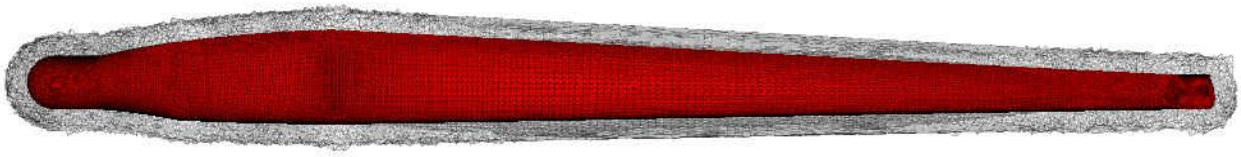

Figure 2. NREL WindPACT-1.5MW wind turbine unstructured blade mesh with 3.24 million nodes.

The near-body mesh flow solver uses a Delayed Detached Eddy Simulation[45] turbulence model, and the off-body adaptive Cartesian mesh solver uses a Constant Smagorinsky Large Eddy Simulation[49] turbulence model. The off-body discontinuous Galerkin flow solver uses $p = 1$, second-order, polynomials in mesh cells near the blade surface and transitions to $p = 3$, fourth-order, polynomials in mesh cells away from the surface with a layer of $p = 2$ mesh cells in between to smoothly transition the solution. The flow solvers use a global time step corresponding to 1/3° rotor rotation, which is followed by flow solution interpolation between the near-body and off-body meshes performed by the overset mesh assembler. The near-body solver performs implicit time steps using the second-order accurate Backwards Difference Formula method, and the off-body uses multiple explicit time steps using the fourth-order accurate Runge-Kutta four-stage method. This spatial and temporal resolution has been determined in previous work[29] as the minimum necessary resolution for ensuring accurate turbine power and thrust predictions.

The simulation is performed without the presence of the wind turbine tower or nacelle. The simulation conditions use uniform inflow, with the fluid parameters set to an ideal fluid (air) of density 1.225 kg/m^3, and a kinematic viscosity of $1.5 \cdot 10^{-5} m^2/s$. The simulation is performed for 50 rotor revolutions starting with 600,000 degrees of freedom in the off-body mesh and grows to over 600 million as the mesh adapts to the wake. The number of cores used for the off-body solver grows to 10,800.

IV. Analysis Approach

Simulation data from the high-fidelity numerical method is collected for 16 rotor revolutions starting at the time step corresponding to the beginning of the 31st rotor revolution, with a temporal resolution based on a time step corresponding to 2° of revolution. This results in a total of 2,880 temporal samples. The spatial samples are taken from two-dimensional cross-wake planes at downstream stations shown in Figure 3, where D denotes rotor diameter. Each plane has a spatial resolution of 400 by 400, which corresponds to a dimensional resolution of 40 cm by 40 cm.

The CFD simulation results are output in the Cartesian coordinate system. Since the simulation does not contain a tower or nacelle, and the inflow is uniform and perpendicular to the rotor plane, the flow is axisymmetric. Since the flow is axisymmetric, a coordinate transformation is applied to the simulation results, and analysis is applied in the polar coordinate system. In the polar reference frame, the velocity vector is composed of axial (denoted U), radial (denoted V), azimuthal (denoted W) components. All results and analysis presented herein are in the polar coordinate system.

V. Results

Figure 3 demonstrates instantaneous axial momentum at multiple downstream stations as a function of rotor diameter (D). Qualitatively, the wake deficit structure is highly regular in the near-wake region starting at the turbine to two rotor diameters (2D) downstream. At station 3D, the wake begins to break down and transition to turbulence as shown in Figure 4, where an instantaneous isocontour of velocity magnitude of 8.5 m/s colored by density demonstrates the tip vortex structure evolution. Between stations 2D and 3D, vortex merging and hopping occur implying instability of the vortex structures. Figure 5 shows an instantaneous flow visualization of the normalized absolute tangential velocity wake structure.

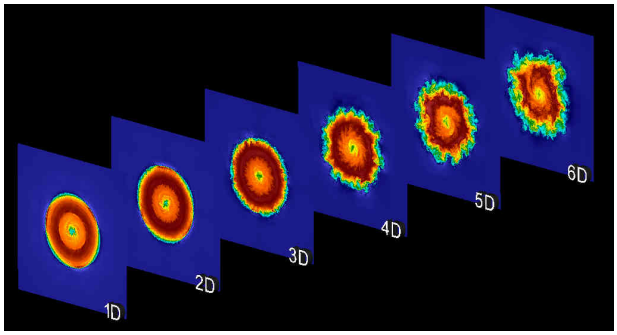

Figure 3. Instantaneous axial momentum at multiple downstream positions of the NREL WindPACT-1.5MW wind turbine.

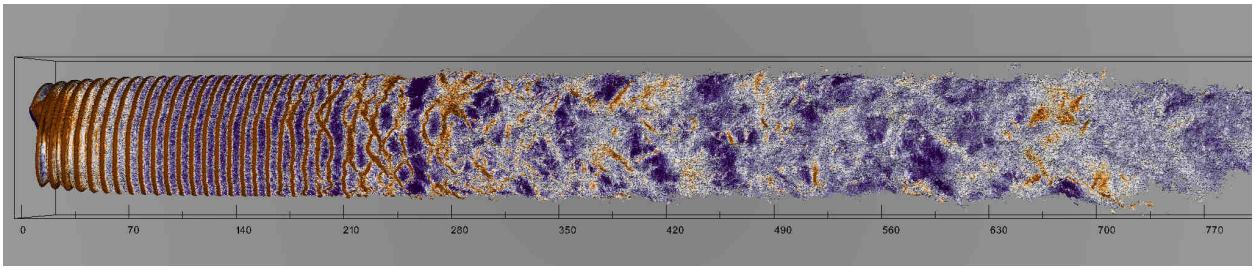

Figure 4. Instantaneous isocontour of the velocity magnitude of 8.5 m/s colored by density demonstrating the vortex structure evolution of the NREL WindPACT-1.5MW wind turbine.

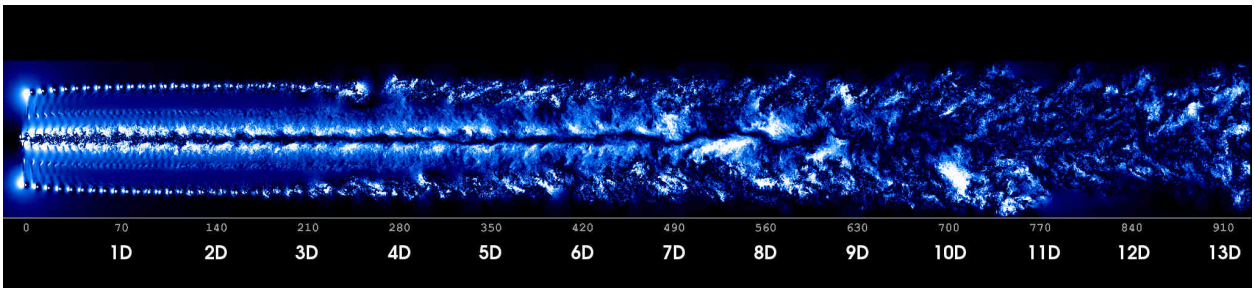

Figure 5. Instantaneous normalized absolute tangential flow velocity demonstrating the wake propagation downstream, annotated by rotor diameter lengths (D).

Figure 6 shows the instantaneous polar velocity components: axial (U), radial (V), and azimuthal (W). The figure shows the flow structures as a function of downstream wake position. The radial velocity is highest near the blade tip regions, whereas the azimuthal velocity is uniformly distributed from the root region out to the blade tip indicating the flow axial induction. Figure 7 demonstrates the time-averaged axial velocity at station x/D = 0.5. The temporal averaging occurred over 16 rotor revolutions of data. The wake is bordered by a sharp transition zone distinguishable by a thin annular area with steep velocity gradient, the shear region. Velocities in the center of the wake are slightly higher since no hub is modeled, and the overall shape of the wake is symmetric, as the turbine tower is also not modeled and the inflow velocity is uniform.

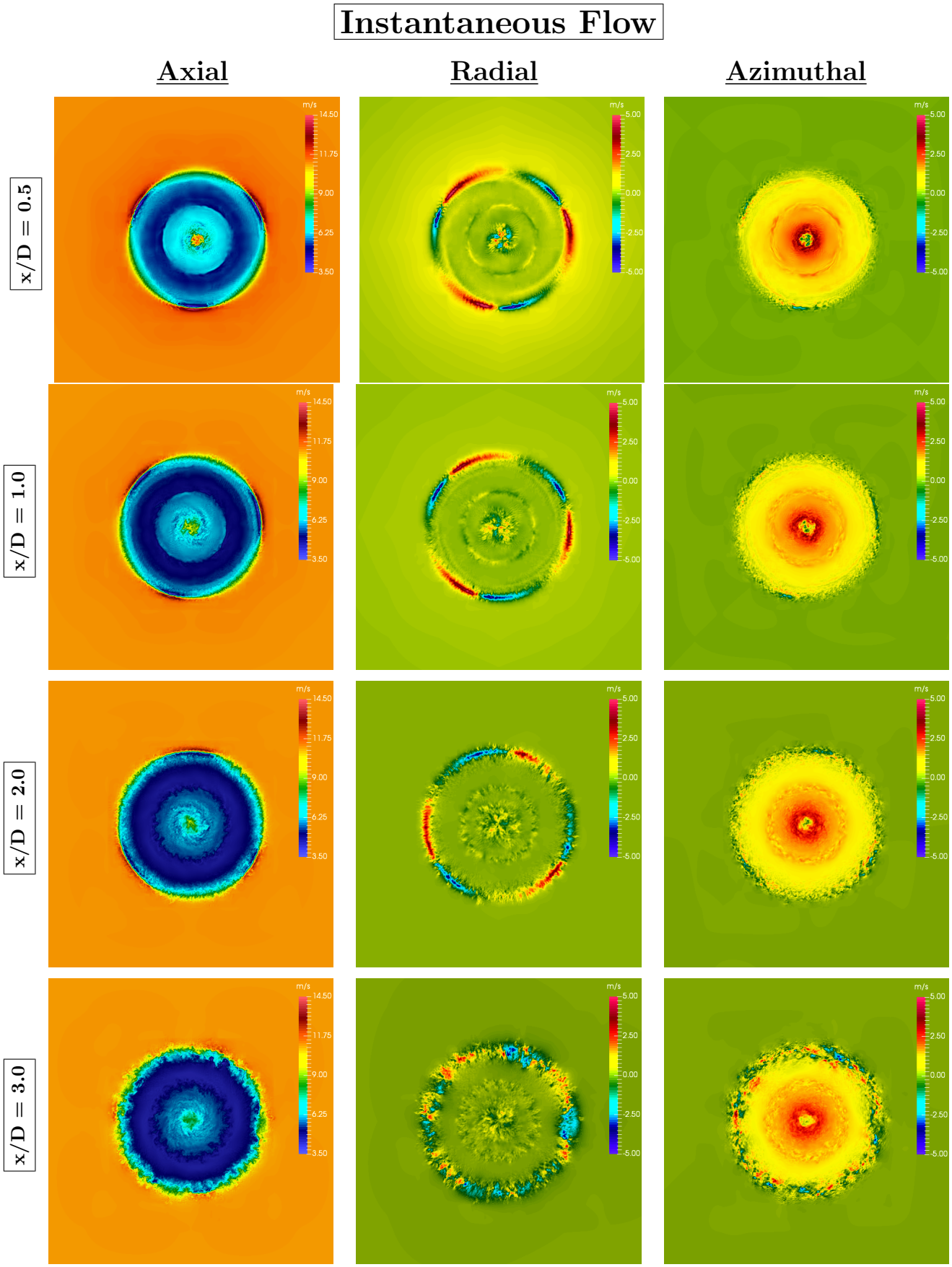

Figure 6. Instantaneous axial (U), radial (V), and azimuthal (W) velocity components at downstream wake positions: 0.5, 1.0, 2.0, and 3.0 rotor diameters (D).

The axial velocity component is determined by a significant velocity deficit caused by the turbine, which gradually recovers to the incoming wind velocity by moving downstream as demonstrated in Figure 8(a). The wake recovery, which is strongly influenced by turbine performance[30] and the incoming turbulent flow,[55] is an important feature for the estimation of the turbine separation distance within a wind farm. The largest velocity deficit is found at the blade tip, r/D = 0.5, where more energy is captured from the flow.[30] Further downstream, this region moves gradually towards the center of the wake. A general radial velocity component near the wake center is observed, which is in agreement with measurements by Medici.[56]

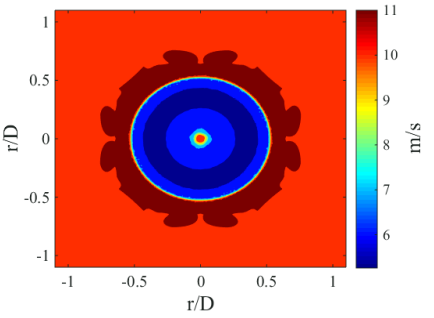

Figure 7. Temporally averaged axial velocity at x/D= 0.5 over 16 rotor revolutions.

However, as seen in Figure 8(b), found by Medici[56] as well, a radial velocity component emerges from the center out to the freestream, which is caused by the centrifugal force applied to the flow in the rotor plane. The radial velocity component reverses towards the center approximately at x/D = 2.0 due to the entrainment from the freestream velocity to the wake. A significant peak of the azimuthal velocity is detected for radial positions r/D = 0.1 shown in Figure 8(c), which is related to the rotational velocity induced by a vorticity structure created in the blade root region. The azimuthal velocity diffuses very slowly as it moves downstream. A feathering is observed for the azimuthal velocity at the r/D = 0.5, influenced by the presence of the tip vortices, which gradually diffuse at downstream distances of approximately x/D = 4.0.

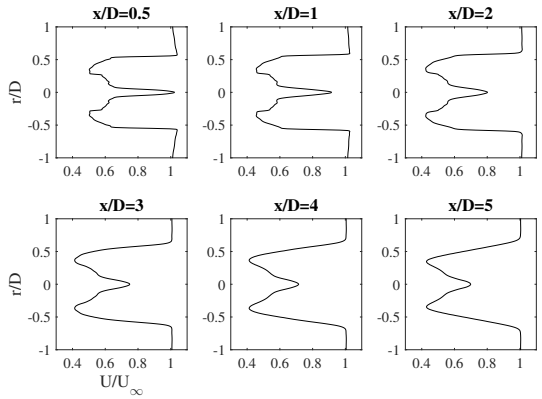

(a) Axial Velocity Deficit

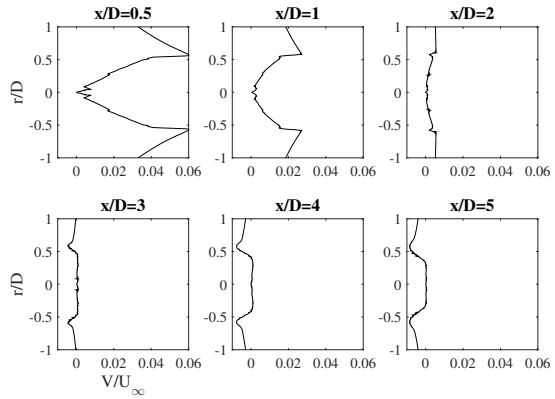

(b) Normalized Radial Velocity

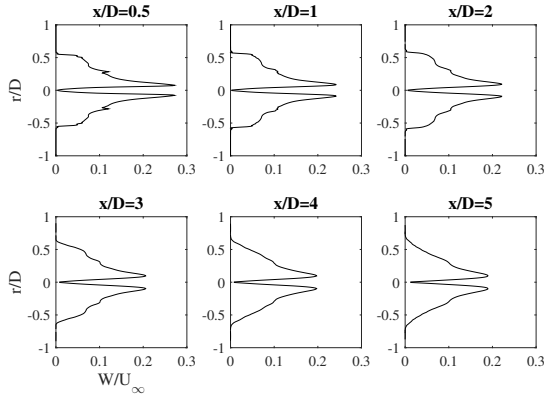

(c) Normalized Azimuthal Velocity

Figure 8. Time-averaged wake velocity profiles normalized by the freestream velocity at different downstream locations.

V.A. Results: Blade

In this section, first-order statistics are analyzed at the wind turbine blade region. Figure 9 demonstrates time history of the calculated dimensional power and thrust for the WindPACT-1.5MW wind turbine. A lower-fidelity model NREL FAST,[57] which couples in an actuator line method, predicts 1.575 megawatts of power and 221,700 Newtons of thrust. The current work predicts the power to be approximately 1.447 megawatts and 212,400 Newtons of thrust.

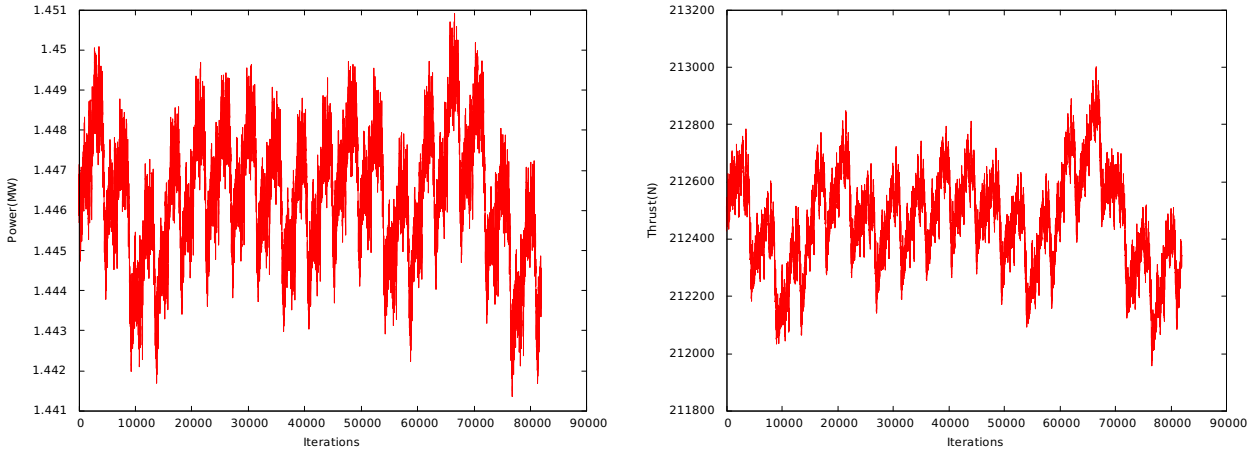

(a) Power (b) Thrust

Figure 9. Power and thrust prediction of the WindPACT-1.5MW wind turbine.

Figure 10 indicates the measurement stations used for blade loadings and coefficient of pressure measurements, which also illustrates the blade geometry. Figure 11 shows the normal (F_n), radial (F_r), tangential (F_θ) loading forces on the blade as a function of normalized radial position. The radial blade forcing is significantly smaller in magnitude than the azimuthal and normal forces. The profile of the radial force transitions from a negative force to a positive force while traversing the first third of the blade radius. As seen in Figure 10, the second station at r/R = 0.13 is positioned on transitioning geometry resulting in a spike in the radial force. The azimuthal force quickly ascends to a plateau from 20% to 90% of the blade radius then quickly falls off. Lastly, the normal blade loading linearly grows as a function of radius and then sharply falls resulting from the generated blade tip vortex. Note that the maximum normal axial force is approximately 8x the maximum azimuthal force and is 80x larger than the maximum radial force.

Figure 12 shows the computed pressure coefficient on the blade surface, and Figure 13 shows the individual station measurements. The sectional coefficient of pressure (C_p) is calculated as follows:

$$C_p = \frac{p - p_\infty}{\frac{1}{2}\rho_\infty \left(U_\infty^2 + (r\omega)^2\right)} \tag{1}$$

where ω is the rotation speed, and r is the sectional radius. The C_p plots indicate well-behaved values along the span of the blade. However, as seen in Figures 12(b) and 13, the pressure side of the wind turbine blade has a region spanning the entire blade where the C_p is negative just behind the leading edge indicating a favorable pressure gradient then transitioning into an adverse pressure gradient. Figure 14 illustrates a blade-tip view of the pressure gradients.

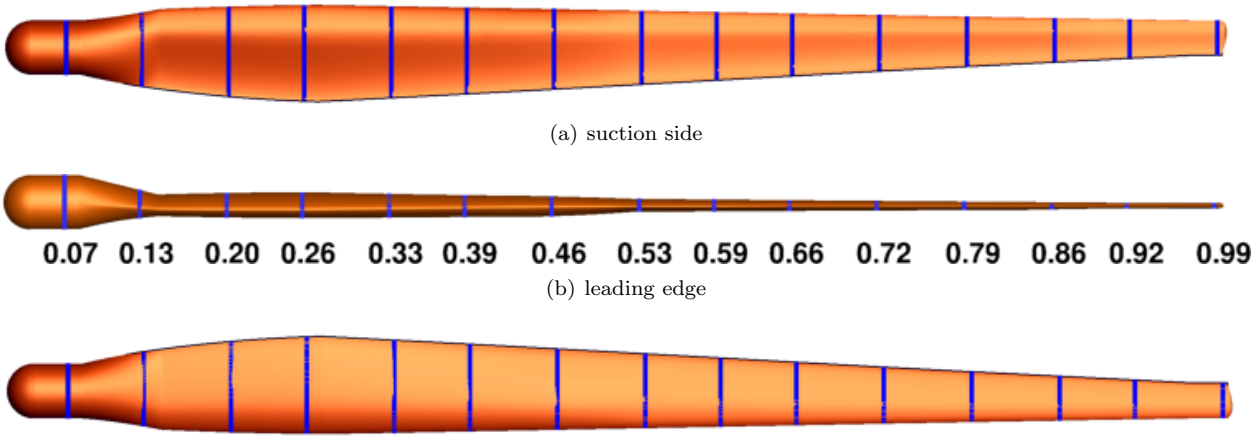

(a) suction side

(b) leading edge

(c) pressure side

Figure 10. Measurement locations for loading forces and coefficient of pressure.

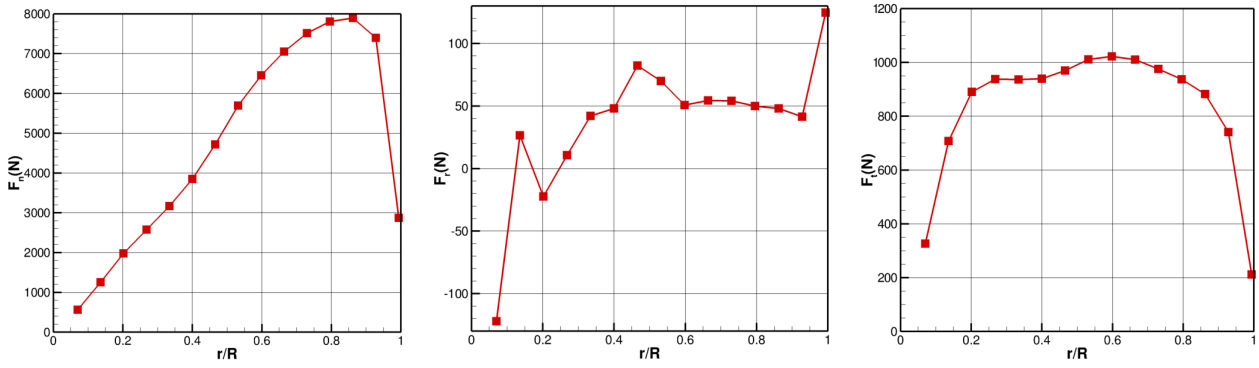

(a) F_n (b) F_r (c) F_θ

Figure 11. Normal [axial] (F_n), radial (F_r), and azimuthal (F_θ) force components distributed along the normalized blade radius.

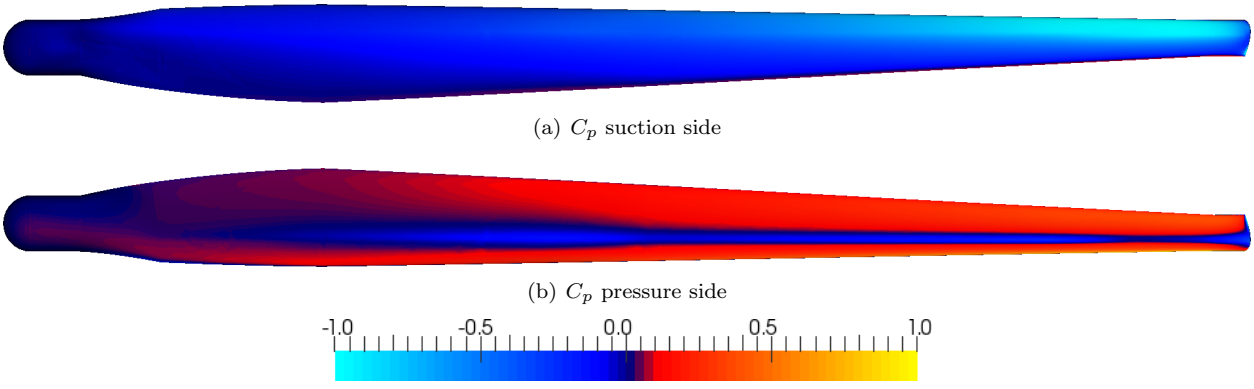

(a) C_p suction side

(b) C_p pressure side

Figure 12. Coefficient of pressure on the blade surface. Pressure gradients are present on the pressure side along the span of the wind turbine blade.

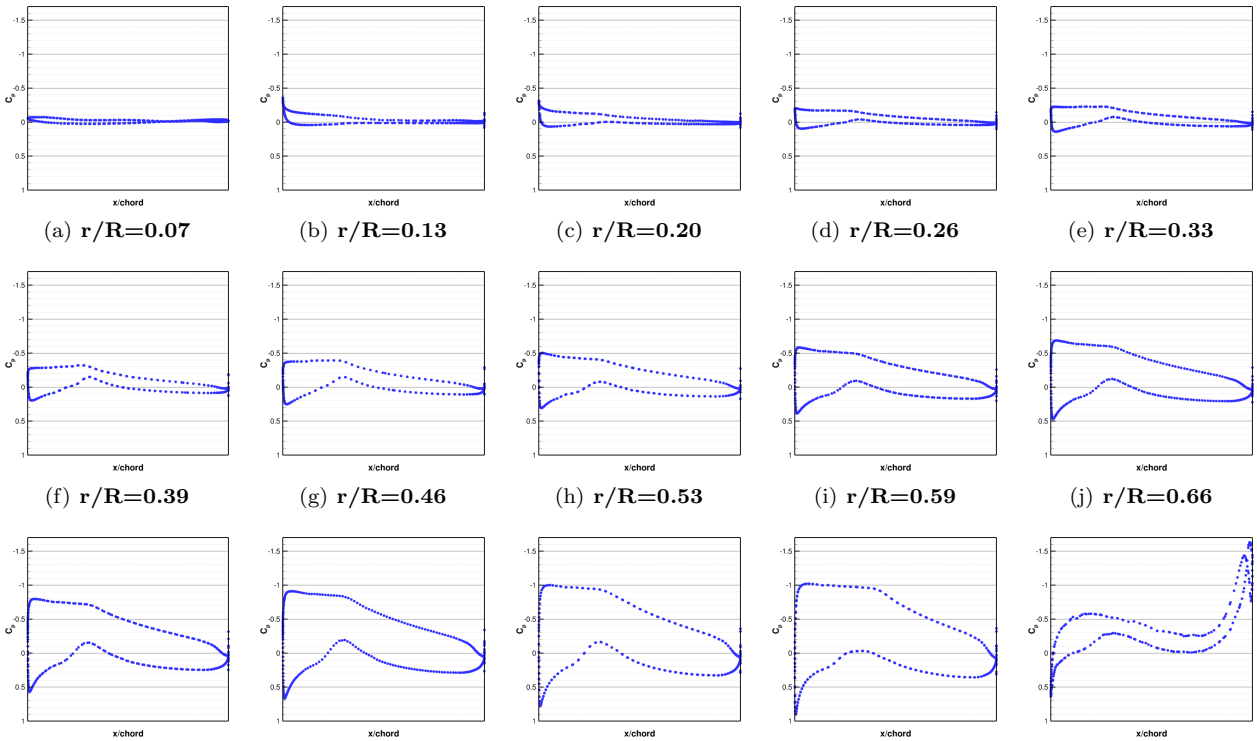

(a) **r/R=0.07** (b) **r/R=0.13** (c) **r/R=0.20** (d) **r/R=0.26** (e) **r/R=0.33**

(f) **r/R=0.39** (g) **r/R=0.46** (h) **r/R=0.53** (i) **r/R=0.59** (j) **r/R=0.66**

(k) **r/R=0.72** (l) **r/R=0.79** (m) **r/R=0.86** (n) **r/R=0.92** (o) **r/R=0.99**

Figure 13. Coefficient of pressure at stations along the blade normalized blade radius.

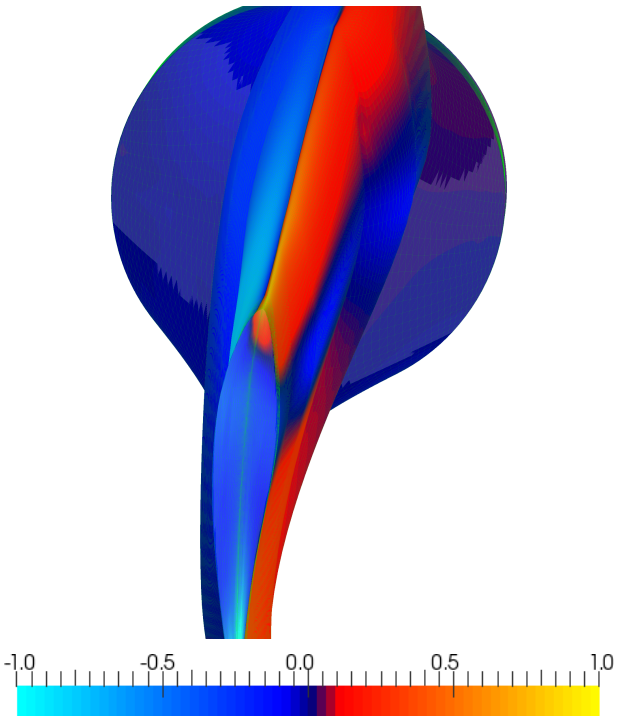

Figure 14. Blade tip view of coefficient of pressure showing pressure gradients spanning the length of the wind turbine blade.

V.B. Results: Reynolds Stress Analysis

In this section,the wake is analyzed in terms of turbulence and Reynolds stresses. First, we denote the instantaneous velocity as $U(t)$ at $t = t_k$ and the temporally-averaged velocity as $\overline{u}$. The Reynolds stresses are averaged temporally over $n = 2,880$ time instances corresponding to 16 rotor revolutions. The Reynolds stresses are calculated as follows:

$$u_i u_j = \frac{\sum_{k=1}^{n} \left(U_i(t_k) - \overline{u}_i\right)\left(U_j(t_k) - \overline{u}_j\right)}{n}, \quad u_i = \{u, v, w\} \tag{2}$$

The normal Reynolds stress uu/U_∞^2, plotted in Figure 15(a), has an increased intensity in the near-wake, representing the mechanically-produced turbulence due to the presence of the wake velocity deficit. This wake turbulent energy gradually dissipates propagating downstream, while the wake diffuses and increases its transverse width. In addition, velocity fluctuations associated with the tip vortices are also detected from the normal stress for locations x/D = 0.5 and 1.0. However, a small increase occurs in the normalized axial stress at x/D = 4.0 and 5.0, which can be due to the divergence of the second-order moments at those locations.

Conversely, in Figure 15(b), the normalized stress connected to the azimuthal velocity component, ww/U_∞^2, corresponding to the outboard of the blade increases downstream. However, the azimuthal normal stress associated with the blade root drops very rapidly in the near wake. Lastly, Figure 15(c) shows the Reynolds shear stress, uw/U_∞^2. This is an important quantity as it is related to the vertical transport of momentum, with negative values of shear indicating entrainment of the freestream flow momentum into the wake, which directly relates to the re-energizing process of the flow.

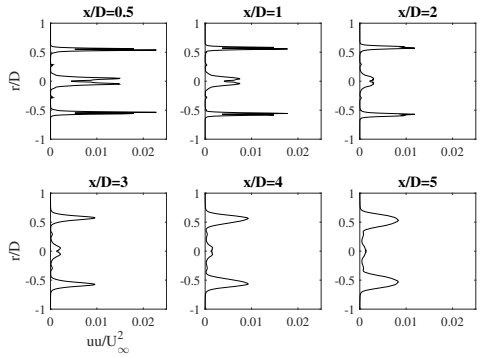

(a) Reynolds normal stress, uu/U_∞^2

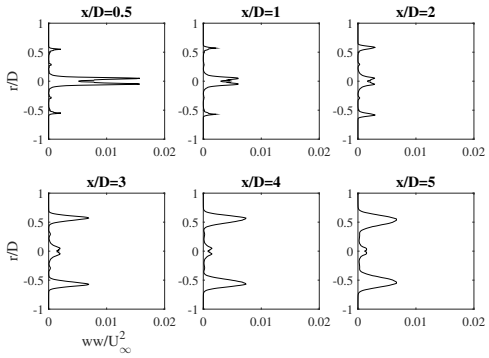

(b) Reynolds normal stress, ww/U_∞^2

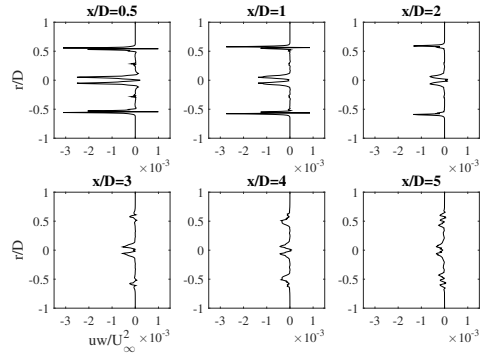

(c) Reynolds shear stress, uw/U_∞^2

Figure 15. Normalized Reynolds stresses at multiple downstream locations.

V.C. Results: Proper Orthogonal Decomposition Analysis

Proper Orthogonal Decomposition (POD) is a common mathematical analysis technique known by other names from other fields (e.g. Principal Component Analysis) and is closely related to singular value decomposition. It is used as a statistical procedure to extract coherent structures within various flows. POD does this by constructing an eigenvector basis to build a modal decomposition from an ensemble of data signals. An eigenvalue problem is solved using a correlation matrix constructed from an autocovariance of the temporal ensemble of velocity snapshots in time, which results in a spatial autocovariance matrix.

First consider a collection of instantaneous flow field snapshots $U(\mathbf{x}, t)$ sampled at m spatial locations and n time instances. The fluctuating (u') and mean ($\overline{u}$) velocity fields are calculated from these n instances as follows:

$$u'(\mathbf{x}, t_j) = U(\mathbf{x}, t_j) - \overline{u}(\mathbf{x}), \quad \text{where } \overline{u}(\mathbf{x}) = \frac{1}{n}\sum_{j=1}^{n} U(\mathbf{x}, t_j) \tag{3}$$

The fluctuating velocity matrix $\boldsymbol{M} \in \mathbb{R}^{(m\times n)}$ is constructed as follows:

$$M_{ij} = u'(x_i, t_j), \quad i = 1, \ldots, m, \; j = 1, \ldots, n \tag{4}$$

The traditional POD method formulates the correlation matrix $\tilde{\boldsymbol{C}} = \frac{1}{n}\boldsymbol{M}\boldsymbol{M}^T \in \mathbb{R}^{(m\times m)}$. From this, an eigenvalue problem is solved as follows:

$$\tilde{\mathbf{C}}\boldsymbol{\phi} = \boldsymbol{\phi}\boldsymbol{\lambda} \tag{5}$$

where $\boldsymbol{\phi} = \phi^l(x_i) \in \mathbb{R}^{(m\times m)}$ is a square matrix whose columns (index l) are the eigenvectors, and $\boldsymbol{\lambda} \in \mathbb{R}^{(m\times m)}$ is a diagonal matrix containing the eigenvalues λ_{ll}. $\boldsymbol{\phi} = \phi^l(x_i)$ are known as the POD modes. The eigenvalues represent the relative kinetic energy in each POD mode, which represent the dominant flow structures. The eigenvalues λ_{ll} are ordered such that:

$$\lambda_1 > \lambda_2 > \ldots > \lambda_m \geq 0 \tag{6}$$

The instantaneous fluctuating velocity field can be represented as a series expansion of POD mode and POD coefficient products. The POD time-varying coefficients are calculated by projecting the velocity fluctuations onto the POD modes as follows:

$$a^l(t_j) = \frac{1}{m}\sum_{i=1}^{m} \phi^l(x_i) \cdot u'(x_i, t_j) \tag{7}$$

Finally, the instantaneous fluctuating velocity can be reconstructed as follows:

$$u'(x_i, t_j) = \sum_{l=1}^{m} a^l(t_j) \cdot \phi^l(x_i) \tag{8}$$

Note that for large data ensembles that have more temporal samples than spatial samples, such as in experimental studies, the traditional POD method is advantageous as the correlation matrix is size $m \times m$, which is smaller than $n \times n$, thus solving the eigenvalue problem in Equation 5 is smaller and easier. However, in computational data, there are generally more spatial samples than temporal samples. Thus, it is advantageous to use the snapshot POD method, which was introduced in 1987 by Sirovich.[33] Snapshot POD, alternatively, solves the eigenvalue problem using the correlation matrix $\boldsymbol{C} = \frac{1}{n}\boldsymbol{M}^T\boldsymbol{M} \in \mathbb{R}^{(n\times n)}$.

Recall, the singular value decomposition (SVD) of a matrix $\boldsymbol{M} \in \mathbb{R}^{(m\times n)}$: $\boldsymbol{M} = \boldsymbol{U}\boldsymbol{\Sigma}\boldsymbol{V}^T$, where $\boldsymbol{U} \in \mathbb{R}^{(m\times m)}$ is a unitary matrix, i.e. $\boldsymbol{U}^T\boldsymbol{U} = \boldsymbol{U}\boldsymbol{U}^T = \boldsymbol{I}$, $\boldsymbol{\Sigma} \in \mathbb{R}^{(m\times n)}$ is a diagonal matrix composed of the singular values of $\boldsymbol{M}$, and $\boldsymbol{V}^T \in \mathbb{R}^{(n\times n)}$ is also a unitary matrix. The matrix $\boldsymbol{U}$ is the set of the orthonormal eigenvectors of $\boldsymbol{M}\boldsymbol{M}^T$, and $\boldsymbol{V}$ is the set of orthornormal eigenvectors of $\boldsymbol{M}^T\boldsymbol{M}$. Further, the diagonal entries $\boldsymbol{\Sigma}$ are the square roots of the non-zero eigenvalues of both $\boldsymbol{M}\boldsymbol{M}^T$ and $\boldsymbol{M}^T\boldsymbol{M}$. Thus, the original POD method solves

for the matrix $\boldsymbol{U}$ and the square values of the matrix $\boldsymbol{\Sigma}$. Alternatively, using the snapshot POD method, one can solve for $\boldsymbol{\Sigma}$ and $\boldsymbol{V}$, then solve for the matrix $\boldsymbol{U}$ by the following procedure:

$$\begin{aligned}
\boldsymbol{M} &= \boldsymbol{U\Sigma V}^T \\
\boldsymbol{MV} &= \boldsymbol{U\Sigma V}^T\boldsymbol{V} && \boxed{\text{right multiply } \boldsymbol{V}} \\
\boldsymbol{MV} &= \boldsymbol{U\Sigma} && \boxed{\boldsymbol{V} \text{ unitary}} \\
\boldsymbol{MV\Sigma}^{-1} &= \boldsymbol{U\Sigma\Sigma}^{-1} && \boxed{\text{right multiply } \boldsymbol{\Sigma}^{-1}} \\
\boldsymbol{MV\Sigma}^{-1} &= \boldsymbol{U} && (9)
\end{aligned}$$

Note that $\boldsymbol{\Sigma}^{-1}$ is nonconventional notation as the matrix is non-square. However, $\boldsymbol{\Sigma}$ is a diagonal matrix with non-zero eigenvalues for the first $\min(m, n)$ entries, thus, reconstruction of the first $\min(m, n)$ columns of the $\boldsymbol{U}$ is as follows:

$$\boldsymbol{U}_l = \frac{1}{\sqrt{\lambda_{ll}}}\boldsymbol{MV}_l \tag{10}$$

Through this process, we are able to solve the eigenproblem of size $\min(m^2, n^2)$ making high spatial resolution simulations tractable for POD using a small number of time samples. Once the eigenvalues and eigenvectors are reconstructed through Equation 10, the process of reconstructing the POD coefficients and velocity fluctuations is analogous to the procedure outlined in Equations 7 and 8.

V.C.1. Results and Analysis

Snapshot POD is applied to the WindPACT-1.5MW wind turbine simulation for an ensemble of data composed of 16 rotor revolutions. The autocovariance matrix is constructed using scalar velocity components, i.e. POD is applied to a single velocity component at a time. The spatial samples are taken from the two-dimensional planes at downstream stations at x/D = 0.5, 1.0, 2.0, and 3.0, as shown in Figures 3.

The POD mode energy is shown in Figure 16 for axial, radial, and azimuthal fluctuating velocity components at multiple downstream stations. The red bars correspond to the mode energy with the mode number as the abscissae. The blue curve represents the accumulating energy as the mode energies are summed. For example, the first six modes for the axial fluctuating velocity at station x/D = 0.5 contain approximately 90% of the fluctuation total energy. The purple dashed line represents the total kinetic energy of the fluctuating velocity; one can compare the kinetic energy of the fluctuating velocity components by reading across each row. The axial fluctuating velocity at x/D = 0.5 has approximately half the energy as the radial fluctuation velocity, but nearly three times the energy of the azimuthal fluctuating velocity.

From Figure 16, the axial and radial fluctuating mode energies are low dimensional in the near-wake region up to station x/D = 2.0 as most energy is contained in the first six modes. Further, strong mode pairs exist (modes 1 and 2, modes 3 and 4) indicating strong flow structure coupling. The azimuthal mode energy is much more distributed as only 70% of the total energy is accounted for in the first 20 modes for station x/D = 0.5 and less than 30% for station x/D = 3.0. At the beginning of the results section, a qualitative observation of the wake appearing to break down in regions between x/D = 2.0 and 3.0 was stated. This observation is confirmed, quantitatively, through the mode energy evolution for all fluctuating velocity components; the mode energy has a significant redistribution from lower modes to higher modes between stations x/D = 2.0 and 3.0. Further, the total energy in the radial component starts very high in comparison to the azimuthal component but loses a third of its energy as the wake moves downstream where a significant increase in the azimuthal mode energy at station 3.0D occurs. This highlights not only a redistribution of energy within its own modes but to other fluctuating velocity components. This confirms the results from the Reynolds stress analysis demonstrating the growth of the azimuthal stress shown in Figure 15(b).

Figure 17 illustrates the POD time-varying coefficients. The amplitudes of the time-varying coefficients demonstrate the mode energy, and the phases demonstrate the pairing. As seen in all fluctuation velocities, pairings between modes 1 and 2 and modes 3 and 4 are present as their respective amplitudes are approximately the same with an approximate 90° phase shift. To further demonstrate this pairing for the axial

fluctuating velocity, Figure 18 shows modes a_2 and a_4 plotted as functions of modes a_1 and a_3, respectively, at stations x/D = 0.5 and 2.0. As the wake moves downstream, we observe this tight coupling between modes begin to deteriorate. This is especially true from station x/D = 2.0 to 3.0. More acutely, the axial time-varying coefficients show an early decoupling in mode pair 3 and 4 at station 2.0D. This decoupling may introduce the energy instability allowing vortex interactions, such as vortex pairing and hopping.

Figure 19 shows a time series of mode 1 for the axial fluctuating velocity at station 0.5D which shows the largest energy containing structure over a period of one rotor revolution. The illustration shows the oscillation of mode 1 changing between positive and negative values at a 60° phase frequency. As a tip vortex passes through the x/D = 0.5 plane, the time-varying coefficient oscillates one full period over 120° of rotation. Thus, for three blades, there are three full periods passing through the wake station plane.

Next, the first 10 POD mode structures at stations 0.5D, 2.0D, and 3.0D are shown in Figures 20, 21, and 22, respectively. Similar mode pairing structures appear in the near-wake region for the axial and radial velocity fluctuations. Most of the structured content is found in the first four modes as asserted by the mode energies. Mode 3 at station 2.0D for the axial component begins to exhibit structural differences compared to its mode pair, mode 4, whereas the radial component still shows strong mode correlation for modes 3 and 4. Significant structure changes emerge at station 3.0D after the initial stages of wake breakdown. The strong asymmetry between axial modes 1 and 2 show a transfer of energy. Particularly, mode 1 of the radial component shows strong negative radial velocity, which indicates strong entrainment from the freestream velocity. More structures appear in higher modes for all three velocity components highlighting that the flow has taken on a higher dimensionality. However, since the wake has begun the transition from near-wake to mid-wake incorporating more turbulent effects, more data is required to assert convergence of the statistics.

VI. Conclusions and Future Work

High-fidelity simulation enables more in-depth capabilities for wind turbine wake analysis. Particularly, blade-resolved simulations allow for the study of the impact of complex aerodynamics on wake characteristics through a first-principles viewpoint. Starting at the wind turbine blade, measurement of the aerodynamic forces and computed pressure coefficients provided insight into the overall wind turbine performance and the evolution of the wake. Reynolds stress analysis highlighted the turbulence quantities responsible for the re-energizing process of the flow in the wake, and Proper Orthogonal Decomposition provided a quantitative and simplified view of the dominant flow structures in the wake with relative energy content. Further, it provided quantitative evidence of the vortex stability breakdown and the wake entrainment process.

Future work will include a computational study of a small-scale wind turbine design matching the non-dimensional force distributions along the wind turbine blade of the NREL WindPACT-1.5MW wind turbine. This will be used to compare and contrast wake characteristics and further explore analysis techniques appropriate for characterizing the relationship of the blade force distributions to wake statistics. POD analysis will be extended to vector quantities for the construction of the autocovariance matrix, relating the cross-velocity component flow structures. Additionally, three-dimensional data will be analyzed using POD to quantify the dominant three-dimensional flow structures.

VII. Acknowledgments

This work is supported in part by ONR Grants N00014-14-1-0045 and N00014-16-1-2737 and by the U.S. Department of Energy, Office of Science, Basic Energy Sciences, under Award DE-SC0012671. The first author was supported in part by the NSF Blue Waters Graduate Fellowship as part of the Blue Waters sustained-petascale computing project, which is supported by the National Science Foundation (awards OCI-0725070 and ACI-1238993).

Computer time was provided by the NCAR-Wyoming Supercomputer Center (NWSC), the University of Wyoming Advanced Research Computing Center (ARCC), and the NSF Blue Waters sustained-petascale computing project.

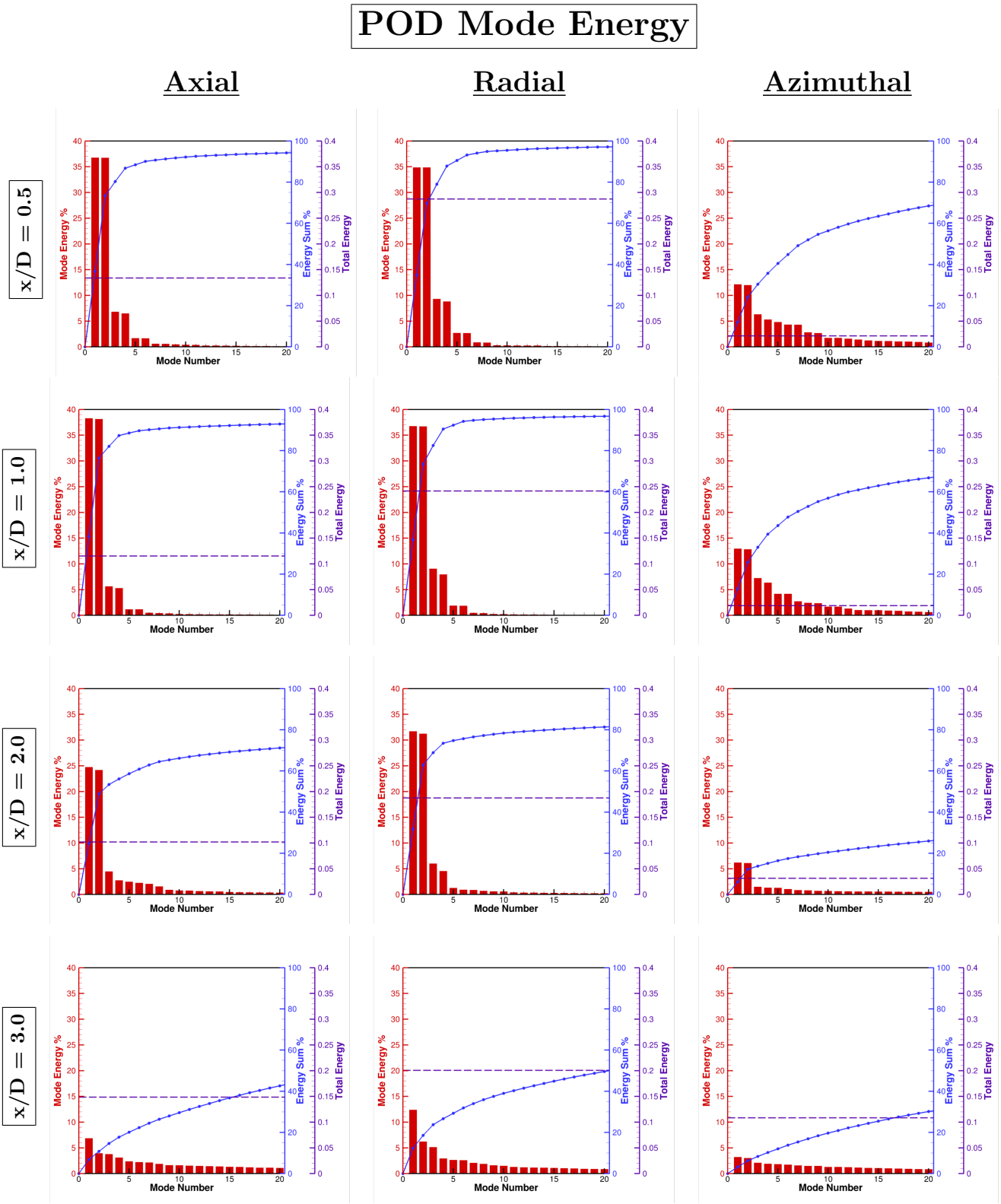

Figure 16. POD mode energies for axial (u'), radial (v'), and azimuthal (w') fluctuation velocities at downstream wake positions.

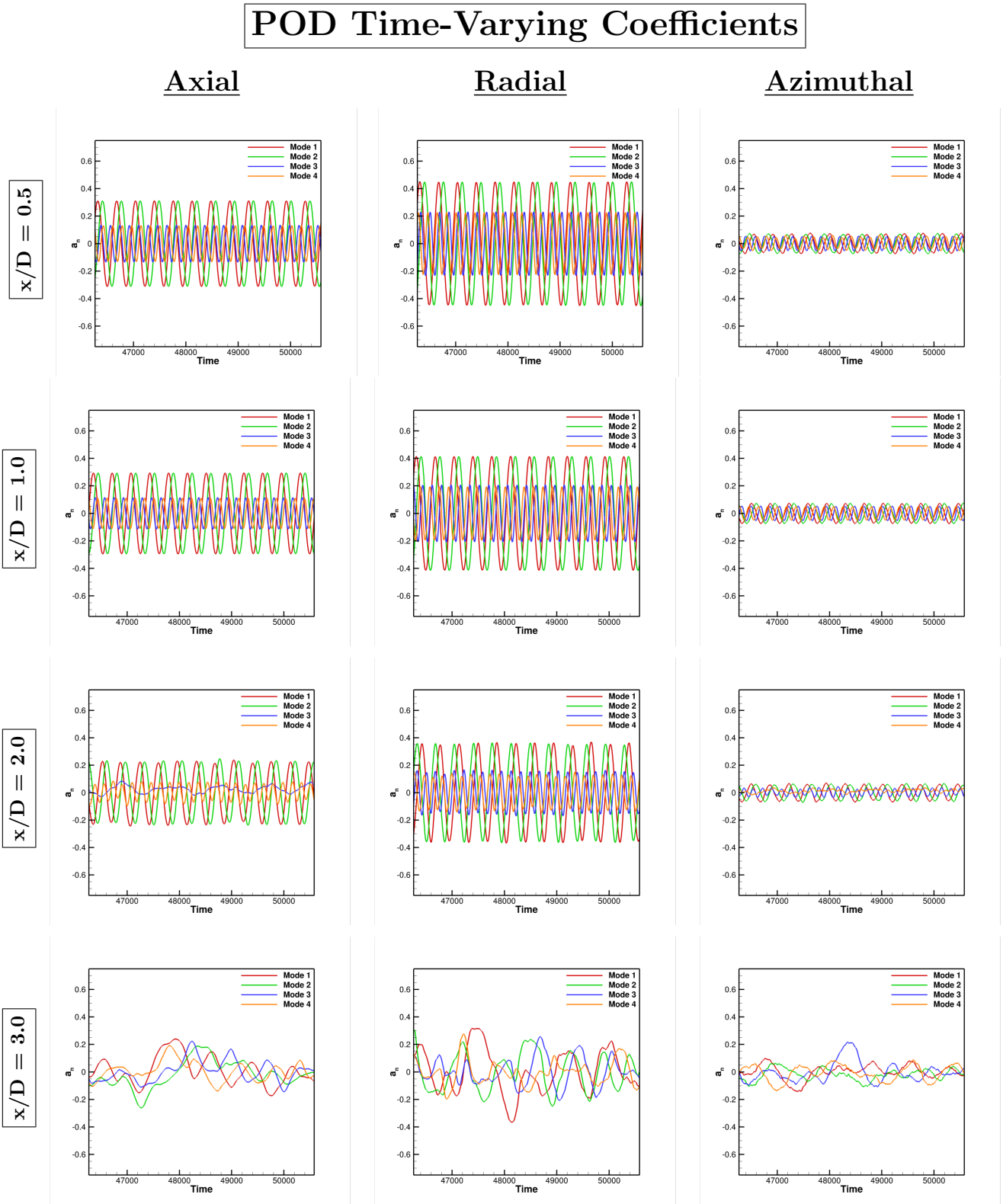

Figure 17. POD time-varying coefficients for u', v', and w' fluctuation velocities at downstream wake positions.

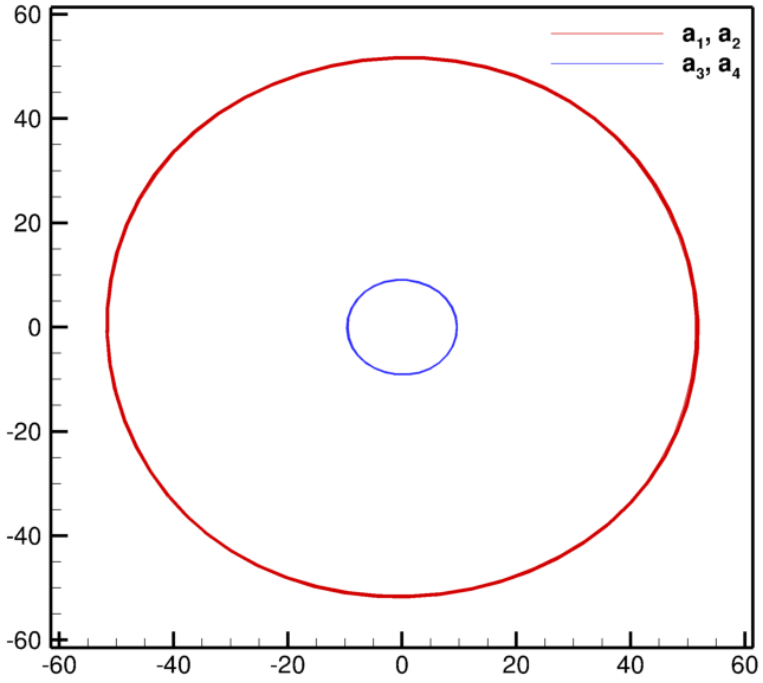

(a) **x/D = 0.5**

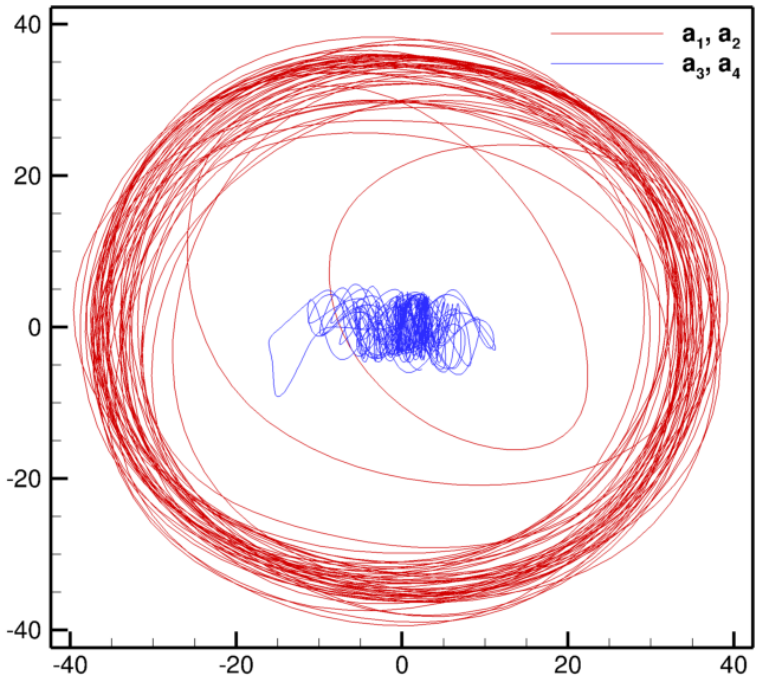

(b) **x/D = 2.0**

Figure 18. Axial fluctuation velocity time-varying coefficient pairings between modes 1 & 2 and modes 3 & 4.

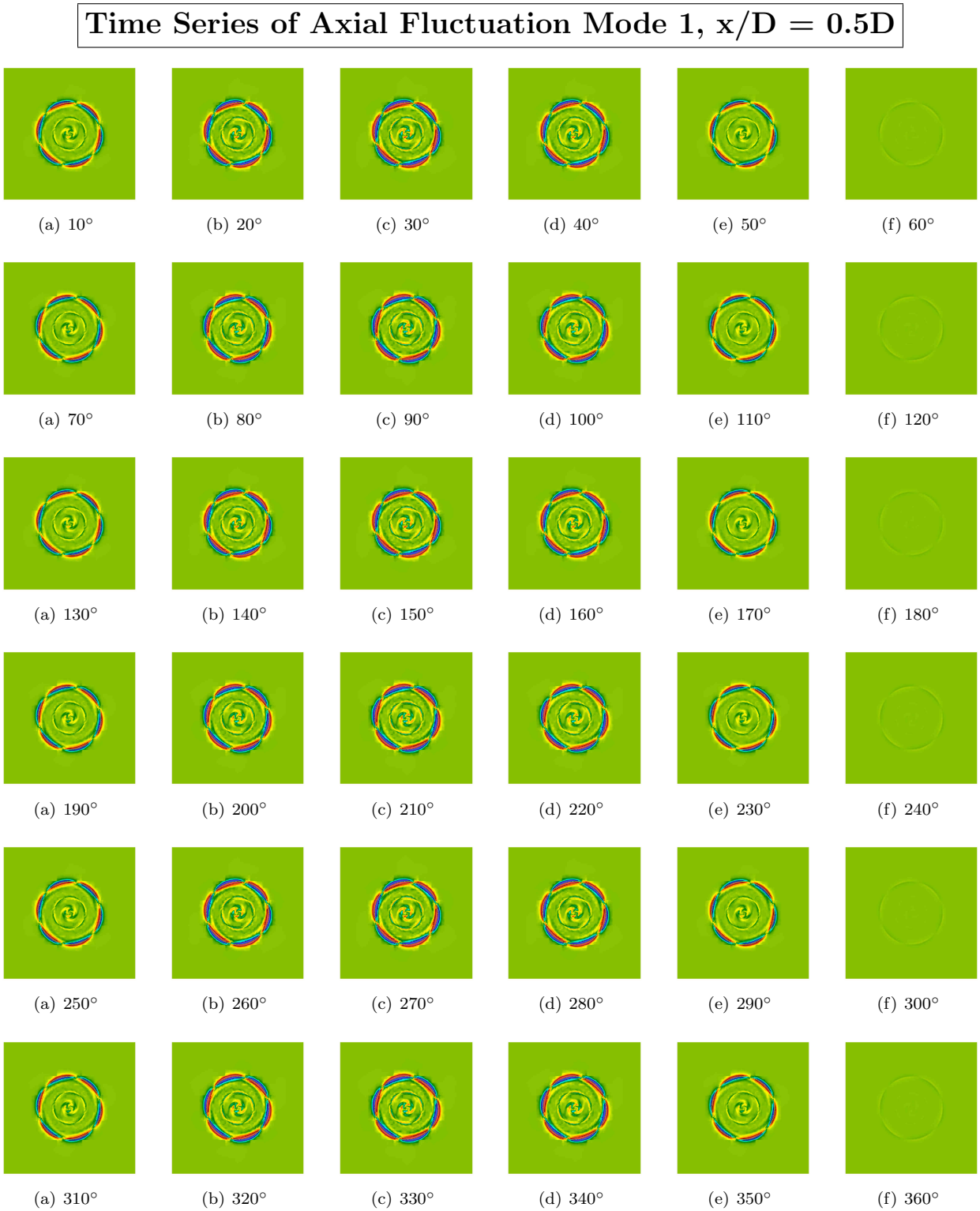

Figure 19. Time series of POD mode 1 for u' at x/D = 0.5D over the period of one rotor revolution.

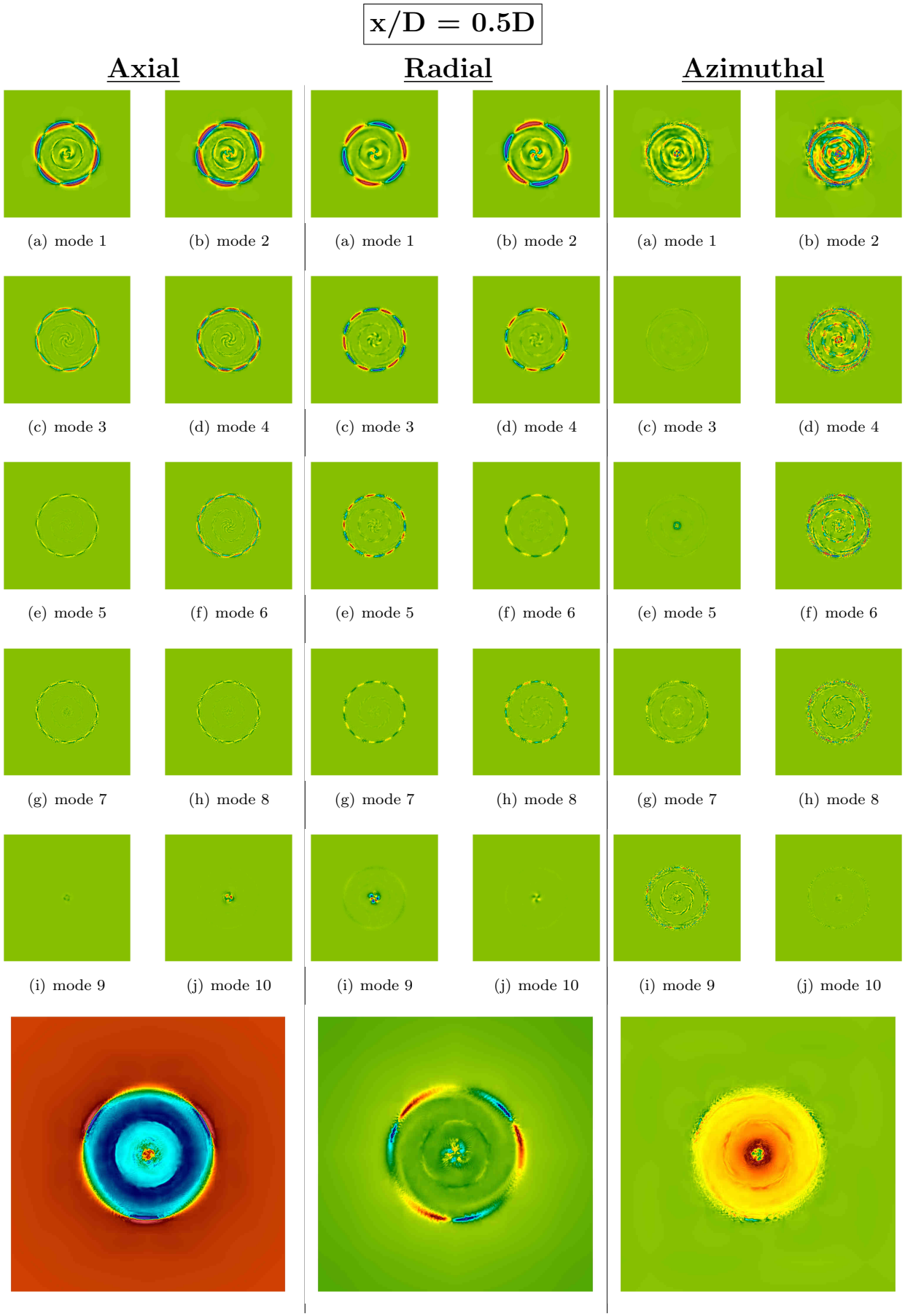

Figure 20. POD modal decomposition and instantaneous flow velocities (bottom) at downstream position x/D = 0.5D.

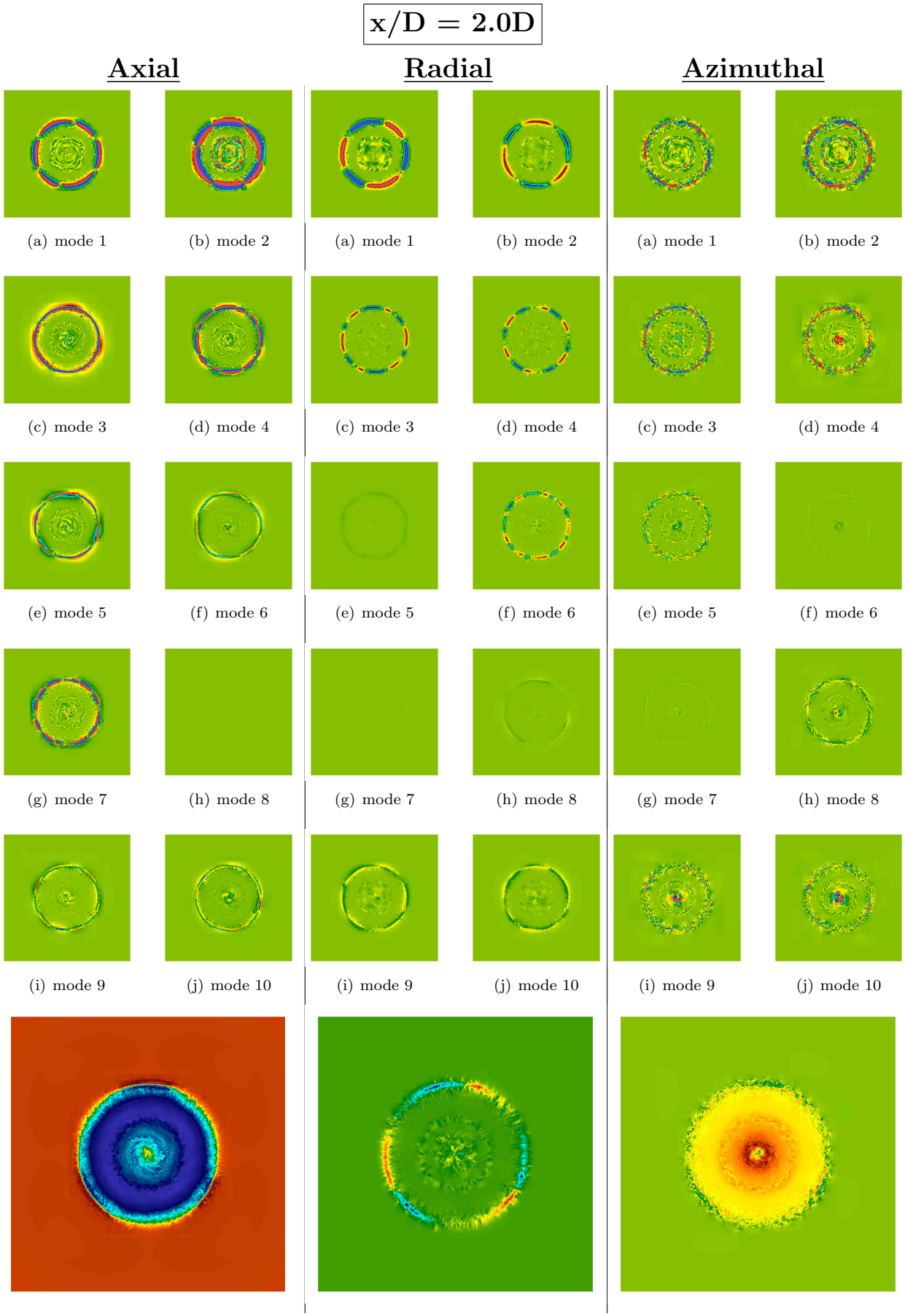

Figure 21. POD modal decomposition and instantaneous flow velocities (bottom) at downstream position x/D = 2.0D.

Figure 22. POD modal decomposition and instantaneous flow velocities (bottom) at downstream position x/D = 3.0D.

References

[1] "Wind Vision: A New Era for Wind Power in the United States," Tech. rep., Technical report, US Department of Energy, Washington, DC, 2015.

[2] Fleming, P., Gebraad, P., van Wingerden, J.-W., Lee, S., Churchfield, M., Scholbrock, A., Michalakes, J., Johnson, K., and Moriarty, P., "SOWFA Super-Controller: A High-Fidelity Tool for Evaluating Wind Plant Control Approaches," Tech. rep., National Renewable Energy Laboratory (NREL), Golden, CO., 2013.

[3] Fleming, P. A., Gebraad, P. M., Lee, S., van Wingerden, J.-W., Johnson, K., Churchfield, M., Michalakes, J., Spalart, P., and Moriarty, P., "Evaluating techniques for redirecting turbine wakes using SOWFA," *Renewable Energy*, Vol. 70, 2014, pp. 211–218.

[4] Gebraad, P., Teeuwisse, F., Wingerden, J., Fleming, P. A., Ruben, S., Marden, J., and Pao, L., "Wind plant power optimization through yaw control using a parametric model for wake effectsa CFD simulation study," *Wind Energy*, Vol. 19, No. 1, 2016, pp. 95–114.

[5] Gebraad, P., Thomas, J. J., Ning, A., Fleming, P., and Dykes, K., "Maximization of the annual energy production of wind power plants by optimization of layout and yaw-based wake control," *Wind Energy*, Vol. 20, No. 1, 2017, pp. 97–107.

[6] Sørensen, J. N. and Myken, A., "Unsteady actuator disc model for horizontal axis wind turbines," *Journal of Wind Engineering and Industrial Aerodynamics*, Vol. 39, No. 1-3, 1992, pp. 139–149.

[7] Mikkelsen, R., *Actuator disc methods applied to wind turbines*, Ph.D. thesis, Technical University of Denmark, 2003.

[8] Troldborg, N., Srensen, J. N., and Mikkelsen, R., "Actuator Line Simulation of Wake of Wind Turbine Operating in Turbulent Inflow," *Journal of Physics: Conference Series*, Vol. 75, No. 1, 2007, pp. 012063.

[9] Churchfield, M., Lee, S., and Moriarty, P., "Overview of the Simulator for Offshore Wind Farm Application SOWFA," 2012.

[10] Churchfield, M., Wang, Q., Scholbrock, A., Herges, T., Mikkelsen, T., and Sjöholm, M., "Using high-fidelity computational fluid dynamics to help design a wind turbine wake measurement experiment," *Journal of Physics: Conference Series*, Vol. 753, IOP Publishing, 2016, p. 032009.

[11] "Top 500, The List: November 2017," 2017, https://www.top500.org/lists/2017/11/.

[12] Duque, E., "Navier-Stokes Analysis of Time-Dependent Flows About Wind Turbine," *Proceedings of the 3rd ASME/JSME joint Fluids Engineering Conference, July18-23, 1999*, 1999.

[13] Takizawa, K., Henicke, B., Tezduyar, T. E., Hsu, M.-C., and Bazilevs, Y., "Stabilized space–time computation of wind-turbine rotor aerodynamics," *Computational Mechanics*, Vol. 48, No. 3, 2011, pp. 333–344.

[14] Bazilevs, Y., Hsu, M.-C., Akkerman, I., Wright, S., Takizawa, K., Henicke, B., Spielman, T., and Tezduyar, T., "3D simulation of wind turbine rotors at full scale. Part I: Geometry modeling and aerodynamics," *International Journal for Numerical Methods in Fluids*, Vol. 65, No. 1-3, 2011, pp. 207–235.

[15] Potsdam, M. A. and Mavriplis, D. J., "Unstructured Mesh CFD Aerodynamic Analysis of the NREL Phase VI Rotor," AIAA Paper 2009-1221, 47th AIAA Aerospace Sciences Meeting, Orlando, FL, January 2009.

[16] Sørensen, N. N., Michelsen, J., and Schreck, S., "Navier-Stokes predictions of the NREL phase VI rotor in the NASA Ames 80 ft× 120 ft wind tunnel," *Wind Energy*, Vol. 5, No. 2-3, 2002, pp. 151–169.

[17] Duque, E. P., Burklund, M. D., and Johnson, W., "Navier-Stokes and comprehensive analysis performance predictions of the NREL phase VI experiment," *Journal of Solar Energy Engineering*, Vol. 125, No. 4, 2003, pp. 457–467.

[18] Pape, A. L. and Lecanu, J., "3D Navier–Stokes computations of a stall-regulated wind turbine," *Wind Energy*, Vol. 7, No. 4, 2004, pp. 309–324.

[19] Gomez-Iradi, S., Steijl, R., and Barakos, G., "Development and Validation of a CFD Technique for the Aerodynamic Analysis of HAWT," *Journal of Solar Energy Engineering*, Vol. 131, No. 3, 2009, pp. 031009.

[20] Zahle, F., Sørensen, N. N., and Johansen, J., "Wind turbine rotor-tower interaction using an incompressible overset grid method," *Wind Energy*, Vol. 12, No. 6, 2009, pp. 594–619.

[21] Bazilevs, Y., Hsu, M.-C., Kiendl, J., Wüchner, R., and Bletzinger, K.-U., "3D simulation of wind turbine rotors at full scale. Part II: Fluid–structure interaction modeling with composite blades," *International Journal for Numerical Methods in Fluids*, Vol. 65, No. 1-3, 2011, pp. 236–253.

[22] Gundling, C., Roget, B., and Sitaraman, J., "Prediction of Wind Turbine Performance and Wake Losses using Analysis Methods of Incremental Complexity," AIAA Paper 2011-458, 49th AIAA Aerospace Sciences Meeting, Orlando, FL, January 2011.

[23] Gundling, C., Roget, B., Sitaraman, J., and Rai, R., "Comparison of Wind Turbine Wakes in Steady and Turbulent Inflow," AIAA Paper 2012-899, 50th AIAA Aerospace Sciences Meeting, Nashville, TN, January 2012.

[24] Rai, R. K., Gopalan, H., Naughton, J. W., and Heinz, S., "A Study of the Sensitivity of Wind Turbine Response to Inflow Temporal and Spatial Scales," 2012.

[25] Li, Y., Paik, K.-J., Xing, T., and Carrica, P. M., "Dynamic overset CFD simulations of wind turbine aerodynamics," *Renewable Energy*, Vol. 37, No. 1, 2012, pp. 285–298.

[26] Yelmule, M. M. and Vsj, E. A., "CFD predictions of NREL phase VI rotor experiments in NASA/AMES wind tunnel," *International Journal of Renewable Energy Research (IJRER)*, Vol. 3, No. 2, 2013, pp. 261–269.

[27] Gopalan, H., Gundling, C., Brown, K., Roget, B., Sitaraman, J., Mirocha, J. D., and Miller, W. O., "A coupled mesoscale–microscale framework for wind resource estimation and farm aerodynamics," *Journal of Wind Engineering and Industrial Aerodynamics*, Vol. 132, 2014, pp. 13–26.

[28] Kirby, A. C., Brazell, M. J., Mavriplis, D. J., and Sitaraman, J., "An Overset Adaptive High-Order Approach for Blade-Resolved Wind Energy Applications," AHS Forum 72, West Palm Beach, FL., May 2016.

[29] Kirby, A. C., Brazell, M. J., Yang, Z., Roy, R., Ahrabi, B. R., Mavriplis, D. J., Sitaraman, J., and Stoellinger, M. K., "Wind Farm Simulations Using an Overset *hp*-Adaptive Approach with Blade-Resolved Turbine Models," AIAA Paper 2017-3958, 23rd AIAA Computational Fluid Dynamics Conference, Denver, CO., June 2017.

[30]Hassanzadeh, A., Naughton, J. W., Kelley, C. L., and Maniaci, D. C., "Wind turbine blade design for subscale testing," *Journal of Physics: Conference Series*, Vol. 753, IOP Publishing, 2016, p. 022048.
[31]Kelley, C. L., Maniaci, D. C., and Resor, B. R., "Scaled Aerodynamic Wind Turbine Design for Wake Similarity," *AIAA 34th Wind Energy Symposium*, Vol. 1521, 2016.
[32]Lumley, J. L., "The structure of inhomogeneous turbulent flows," *Atmospheric turbulence and radio wave propagation*, 1967.
[33]Sirovich, L., "Turbulence and the dynamics of coherent structures. I. Coherent structures," *Quarterly of applied mathematics*, Vol. 45, No. 3, 1987, pp. 561–571.
[34]Berkooz, G., Holmes, P., and Lumley, J. L., "The proper orthogonal decomposition in the analysis of turbulent flows," *Annual review of fluid mechanics*, Vol. 25, No. 1, 1993, pp. 539–575.
[35]Willcox, K. and Peraire, J., "Balanced model reduction via the proper orthogonal decomposition," *AIAA journal*, Vol. 40, No. 11, 2002, pp. 2323–2330.
[36]Andersen, S. J., Sørensen, J. N., and Mikkelsen, R., "Simulation of the inherent turbulence and wake interaction inside an infinitely long row of wind turbines," *Journal of Turbulence*, Vol. 14, No. 4, 2013, pp. 1–24.
[37]Bastine, D., Witha, B., Wächter, M., and Peinke, J., "POD analysis of a wind turbine wake in a turbulent atmospheric boundary layer," *Journal of Physics: Conference Series*, Vol. 524, IOP Publishing, 2014, p. 012153.
[38]Durgesh, V. and Naughton, J. W., "Multi-time-delay LSE-POD complementary approach applied to wake flow behind a bluff body," *ASME Paper FEDSM2007-37175*, 2007.
[39]Brazell, M. J., Kirby, A. C., and Mavriplis, D. J., "A high-order discontinuous-Galerkin octree-based AMR solver for overset simulations," AIAA Paper 2017-3944, 23rd AIAA Computational Fluid Dynamics Conference, Denver, CO., June 2017.
[40]Brazell, M. J., Kirby, A. C., Sitaraman, J., and Mavriplis, D. J., "A multi-solver overset mesh Approach for 3D mixed element variable order discretizations," AIAA Paper 2016-2053, 54th AIAA Aerospace Sciences Meeting, San Diego, CA., June 2016.
[41]Mavriplis, D. J., "Grid resolution study of a drag prediction workshop configuration using the NSU3D unstructured mesh solver," AIAA Paper 2005-729, 23rd AIAA Applied Aerodynamics Conference, Toronto, Ontario Canada, June 2005.
[42]Mavriplis, D. and Long, M., "NSU3D Results for the Fourth AIAA Drag Prediction Workshop," *Journal of Aircraft*, Vol. 51, No. 4, 2014, pp. 1161–1171.
[43]Spalart, P. and Allmaras, S., "A one-equation turbulence model for aerodynamic flows," *30th aerospace sciences meeting and exhibit*, 1992, p. 439.
[44]Wilcox, D. C., "Reassessment of the scale-determining equation for advanced turbulence models," *AIAA journal*, Vol. 26, No. 11, 1988, pp. 1299–1310.
[45]Spalart, P. R., Deck, S., Shur, M., Squires, K., Strelets, M. K., and Travin, A., "A new version of detached-eddy simulation, resistant to ambiguous grid densities," *Theoretical and computational fluid dynamics*, Vol. 20, No. 3, 2006, pp. 181–195.
[46]Shur, M. L., Strelets, M. K., Travin, A. K., and Spalart, P. R., "Turbulence modeling in rotating and curved channels: assessing the Spalart-Shur correction," *AIAA journal*, Vol. 38, No. 5, 2000, pp. 784–792.
[47]Burstedde, C., Ghattas, O., Gurnis, M., Isaac, T., Stadler, G., Warburton, T., and Wilcox, L., "Extreme-scale AMR," *Proceedings of the 2010 ACM/IEEE International Conference for High Performance Computing, Networking, Storage and Analysis*, IEEE Computer Society, 2010, pp. 1–12.
[48]Burstedde, C., Wilcox, L. C., and Ghattas, O., "p4est: Scalable algorithms for parallel adaptive mesh refinement on forests of octrees," *SIAM Journal on Scientific Computing*, Vol. 33, No. 3, 2011, pp. 1103–1133.
[49]Smagorinsky, J., "General circulation experiments with the primitive equations: I. The basic experiment," *Monthly weather review*, Vol. 91, No. 3, 1963, pp. 99–164.
[50]Roget, B. and Sitaraman, J., "Robust and efficient overset grid assembly for partitioned unstructured meshes," *Journal of Computational Physics*, Vol. 260, 2014, pp. 1–24.
[51]Brazell, M. J., Sitaraman, J., and Mavriplis, D. J., "An overset mesh approach for 3D mixed element high-order discretizations," *Journal of Computational Physics*, Vol. 322, 2016, pp. 33–51.
[52]Crabill, J. A., Sitaraman, J., and Jameson, A., "A High-Order Overset Method on Moving and Deforming Grids," *AIAA Modeling and Simulation Technologies Conference*, 2016, p. 3225.
[53]"Wind Partnerships for Advanced Component Technology: Windpact Advanced Wind Turbine Drivetrain Designs," *U.S. Dept. of Energy, Energy Efficiency and Renewable Energy*, 2006.
[54]Malcolm, D. and Hansen, A., "WindPACT turbine rotor design study," *National Renewable Energy Laboratory, Golden, CO*, Vol. 5, 2002.
[55]Khan, M., Odemark, Y., and Fransson, J. H., "Effects of Inflow Conditions on Wind Turbine Performance and near Wake Structure," *Open Journal of Fluid Dynamics*, Vol. 7, 2017, pp. 105–129.
[56]Medici, D., *Experimental studies of wind turbine wakes: power optimisation and meandering*, Ph.D. thesis, KTH, 2005.
[57]Jonkman, J. M. and Buhl Jr, M. L., "FAST User's Guide-Updated August 2005," Tech. rep., National Renewable Energy Laboratory (NREL), Golden, CO., 2005.